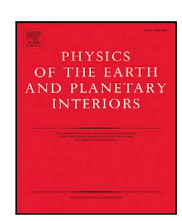
FISEVIER

Contents lists available at ScienceDirect

Physics of the Earth and Planetary Interiors

journal homepage: www.elsevier.com/locate/pepi



Core field changes from eleven years of *Swarm* satellite observations[☆]

C.C. Finlay ^{a, *}, C. Kloss ^a, N. Gillet ^b

- ^a Divsion of Geomagnetism and Geospace, Department of Space Research and Technology, Technical University of Denmark, Building 356, Lyngby, 2800, Copenhagen, Denmark
- b IsTerre, Université, Grenoble Alpes, Université, Savoie Mont Blanc, CNRS, IRD, UGE, Grenoble, F-38000, France

ARTICLE INFO

Dataset link: https://swarm-diss.eo.esa.int/, https://data.dtu.dk/

Keywords: Earth's magnetic field Secular variation Swarm satellite mission Geodynamo

ABSTRACT

The *Swarm* satellite trio has provided global vector magnetic field measurements, with high precision and absolute accuracy, for the past eleven years. Based on this consistent, high quality, dataset we describe here how Earth's main (core-generated) magnetic field has evolved between 2014.0 and 2025.0.

At the Earth's surface, we find that the region in the South Atlantic where the field strength is weakest (below 26,000 nT), has expanded by 0.9% of Earth's surface area and that the minimum intensity has decreased by 336 nT from 22,430 nT to 22,094 nT. In the northern polar region, we find that in Canada the area of strong field (above 57,000 nT) has diminished, decreasing in size by 0.65% of Earth's surface area and with the maximum field strength decreasing by 801 nT from 58,832 nT to 58,031 nT. In contrast the corresponding strong field region in Siberia has grown in size, increasing in area by 0.42% of Earth's surface area, with the maximum field intensity increasing by 260 nT from 61,359 nT to 61,619 nT.

At the core-mantle boundary, reversed flux features under southern Africa have moved westward, converging towards reversed flux features that have moved eastwards under the mid-Atlantic. In the northern polar region a strong flux feature under the Bering strait has moved westwards along the inner-core tangent cylinder. At low latitudes, under Indonesia and the western Pacific, field features have surprisingly moved eastwards. Field accelerations, including oscillations, are found to be most intense at low latitudes.

The Swarm mission has for the past decade been an essential source of global information on the changes taking place in Earth's main magnetic field. Due to the long timescales of the underlying core processes, extending the mission lifetime for as long as possible, in particular for the higher satellite Swarm Bravo, is expected to yield further scientific insights. A long mission for Swarm Bravo would be an efficient means of ensuring that the present era of high quality geomagnetic observations from space continues as new missions come online.

1. Introduction

The Swarm satellite mission (Friis-Christensen et al., 2006; Olsen and Floberghagen, 2018) has provided high precision vector measurements of Earth's magnetic field, with absolute accuracy, since November 2013. The three Swarm satellites, known as Alpha, Bravo and Charlie, each carry identical instrumentation. The magnetometry package includes crucial fluxgate Vector Field Magnetometers (Primdahl and Jensen, 1982; Brauer et al., 2001; Merayo et al., 2008), connected by a rigid optical bench to Star Trackers that provide attitude information (Jørgensen et al., 2001), and Absolute Scalar Magnetometers (Leger et al., 2009) that ensure absolute accuracy. More than 11 years of observations are now available from the Swarm satellites, making this the longest series of continuous, absolute accuracy, magnetic measurements from low-Earth-orbit by the same instruments,

surpassing the ten-year record provided by the CHAMP mission. Thanks to the ongoing efforts of ESA and the Swarm DISC group (Olsen et al., 2013; Swarm DISC, 2025) there is excellent data availability over the entire timespan of the mission. The unique global magnetic record provided by *Swarm* enables us to analyse in detail how the Earth's magnetic field has evolved since its launch. This has led to a re-assessment of existing ideas concerning the origin of geomagnetic secular variation, and has provided new insights into the underlying core dynamics (e.g. Gillet et al. (2022), Finlay et al. (2023)).

This article is an extended written version of a presentation made at the *Swarm* 10 year Anniversary meeting in Copenhagen in April 2024, which summarized the changes in Earth's core-generated magnetic field that have been observed by the *Swarm* satellites. In order to document the changes in the core magnetic field seen by *Swarm* we present here

E-mail address: cfinlay@space.dtu.dk (C.C. Finlay).

This article is part of a Special issue entitled: 'Terr. Magnetism & Swarm' published in Physics of the Earth and Planetary Interiors.

^{*} Corresponding author.

a new geomagnetic field model, focusing on the time-dependent core field. In contrast to other field models (e.g. Sabaka et al. (2020), Finlay et al. (2020), Baerenzung et al. (2022)) we use observations only from the *Swarm* mission and not from earlier magnetic survey missions, ground observatories or calibrated platform magnetometers. Although this restricts the time-interval studied it provides a dataset that is more uniform in space and time and is derived from a single instrumentation package. Our field modelling method is specifically designed for study of the core field and makes use of physically-motivated spatial and temporal regularizations imposed at the core-mantle boundary using techniques developed by Otzen et al. (2024) and Gillet et al. (2024) respectively.

We begin by studying the field at Earth's surface, and initially focus on the recent evolution of the well known weak field region in the South Atlantic. This South Atlantic Anomaly (SAA) has been recognized since the 19th century, based on important early work by Humboldt, Hansteen, Gauss and others in producing the first maps of the magnetic field intensity (see, for example Reich and Roussanova (2015)). Later, at the dawn of the space age, the SAA was found to have important implications for the near-Earth radiation environment (Ginzburg et al., 1962; Vernov and Chudakov, 1960; Yoshida et al., 1960). Today the SAA is known to be an major factor in determining the radiation dose experienced by low Earth orbit satellites and its ongoing evolution is of considerable interest both to space physicists and satellite engineers.

We also investigate changes in the Canadian and Siberian strong field regions at Earth's surface. The fact that there are two maxima of field intensity in the northern hemisphere (in Canada and Siberia) was first pointed out by Hansteen (1819), (see also Brekke and Egeland, 1986). In contrast there only is a single maxima of field intensity in the Southern hemisphere, located south of Australia. This hemispherical asymmetry in the field intensity provides important clues regarding the core dynamo process currently generating and maintaining the field; changes in the relative amplitudes of the two northern hemisphere maxima are thus of fundamental interest. Changes in the Canadian and Siberian field maxima are also crucial for Arctic navigation as they affect both the magnetic declination and the magnetic dip pole position (Alken et al., 2021; Livermore et al., 2020). In addition to documenting changes in these features at Earth's surface during the Swarm era, we also examine their origin at the core-mantle boundary.

In Section 2 we describe how we reduce the *Swarm* measurements to a geomagnetic field model, and document how we thereby isolate the field generated in the core. In Section 3 we document the details of *Swarm* satellite data used. In Section 4 we present our results concerning the changes in the core field at Earth's surface and at the core-mantle boundary. A discussion and conclusions are offered in Section 5.

2. Field modelling methodology

2.1. Forward modelling

We follow the conventional approach and represent the magnetic field as the gradient of a scalar potential V due to internal and external sources (e.g. Backus et al. (1996), Sabaka et al. (2015)) such that

$$\mathbf{B} = -\nabla V \qquad \text{where} \quad V = V^{int} + V^{ext}, \tag{1}$$

The potential V^{int} due to internal sources is parameterized as

$$V^{int}(r,\theta,\phi) = a \sum_{n=1}^{N_C} \left(\frac{a}{r}\right)^{n+1} \sum_{m=0}^{n} \left[g_C^{n,m}(t) \cos m\phi + h_C^{n,m}(t) \sin m\phi \right] P_n^m(\cos\theta)$$

$$+ a \sum_{n=1}^{N_L} \left(\frac{a}{r}\right)^{n+1} \sum_{n=0}^{n} \left[g_L^{n,m} \cos m\phi + h_L^{n,m} \sin m\phi \right] P_n^m(\cos\theta)$$
 (2)

where (r, θ, ϕ) are geocentric spherical polar co-ordinates, a is the Earth's mean spherical reference radius, n is the degree of the spherical harmonic, m the order of the spherical harmonic and $P_n^m(\cos \theta)$ are

associated Legendre functions. Following Otzen et al. (2024) we define separate spherical harmonic (or Gauss) coefficients for the lithospheric field $(g_L^{n,m}$ and $h_L^{n,m}$), assumed here to be static and considered up to a maximum degree $N_L=80$, and for the time-dependent core field $(g_C^{n,m}(t))$ and $h_C^{n,m}(t)$, considered here up to a maximum degree $N_C=22$. The core field coefficients are further expanded in time using a B-spline basis, of order 6 and with a 0.5 year knot spacing as

$$g_C^{n,m}(t) = \sum_k g_C^{n,m,k} B_k(t),$$
 (3)

where $\mathcal{B}_k(t)$ are localized spline basis functions that together cover the eleven year timespan from 2014.0 to 2025.0. $g_C^{n,m,k}$ are the spline coefficients that parameterize the time-dependent Gauss coefficients of the core field. Note that the core and lithospheric field models in Eq. (2) are colinear. In order to distinguish between these two internal sources, we make use of additional information concerning (i) the depth of the sources, and (ii) the expected spatial correlations at each source surface. This information is used to define measures of the information entropy which are maximized during the field estimation procedure. Further details regarding our choice of prior information and synthetic tests of its performance can be found in Otzen et al. (2024); details of the specific implementation used here are given in the following section.

For the parameterization of the external field we adopt the formalism of the CHAOS series of field models (see Olsen et al., 2014, for more details)). This includes an expansion of the external dipole field in SM (Solar Magnetic) coordinates, with time-dependence given by the ground-observatory based RC index (which describes hourly time-variations of the magnetospheric Ring Current) with scaling coefficients and time-varying offsets solved for in 30 day bins. In addition there is an expansion of fields that are stationary in GSM (Geocentric Solar Magnetospheric) coordinates. Associated fields induced in the electrically-conducting solid Earth are calculated using an a-priori conductivity model consisting of a mantle with 1-D (radial) conductivity distribution (Grayver et al., 2017) overlaid by a surface layer of laterally-variable conductance as described in Finlay et al. (2020).

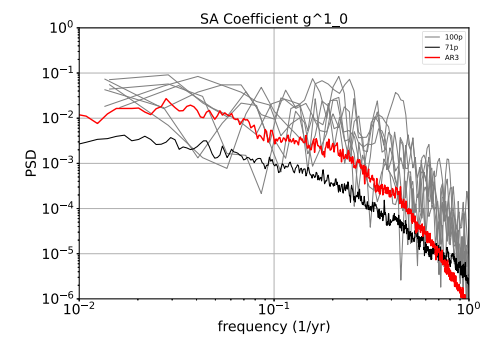
In addition to parameterizing internal and external potential field sources we also co-estimated Euler angles describing the rotation of the vector magnetic field from the magnetometer frame to the satellite frame, allowing these to vary in 30 day bins. In all our model consists of 22,434 model parameters, hereafter denoted by the vector \mathbf{m} . 14,256 coefficients describe the time-dependent core field model and are denoted by \mathbf{m}_C . 6560 static spherical harmonic coefficients describe the lithospheric field and are denoted by \mathbf{m}_L . 412 parameters describe the time-varying external field and the remaining 1206 parameters are Euler angles used to perform in-flight estimation of the magnetometer alignment (Olsen et al., 2006). We estimate all these model parameters simultaneously from the eleven years of Swarm data described below in Section 3.

2.2. Model estimation

For estimation of the model coefficients we use a gradient descent algorithm that iteratively minimizes the loss function

$$\boldsymbol{\Phi}(\mathbf{m}) = \frac{1}{2} \chi^2(\mathbf{m}) - S(\mathbf{m}_L) - S_{tav}(\mathbf{m}_C) + \frac{1}{2} \mathbf{m}_C^T \boldsymbol{\Lambda}_t \mathbf{m}_C + \frac{1}{2} \mathbf{m}_C^T \boldsymbol{\Lambda}_2 \mathbf{m}_C + \frac{1}{2} \mathbf{m}^T \boldsymbol{\Lambda}_a \mathbf{m}_C$$
(4)

The term denoted χ^2 measures the data misfit. $-S(\mathbf{m}_L)$ and $-S_{tav}(\mathbf{m}_C)$ are information entropy-based measures used to spatially regularize the lithospheric and core fields respectively at the Earth's surface and at the core-mantle boundary (negative signs are because we seek to maximize the entropy, see Section 2.2.2 below). Temporal regularization is enforced through the term $\mathbf{m}_C^T \mathbf{\Lambda}_t \mathbf{m}_C$ where $\mathbf{\Lambda}_t = \mathbf{G}_t^T \ddot{\mathbf{C}}_t^{-1} \mathbf{G}_t$ with $\ddot{\mathbf{C}}_t$ an a-priori temporal covariance matrix for the spherical harmonic



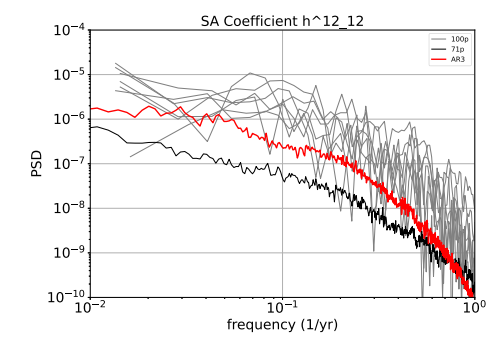


Fig. 1. Power spectral density of example secular acceleration (SA) coefficients from the 71p geodynamo simulation (black) and 7 shorter realizations of the 100p geodynamo simulation (grey) together with that from the estimated AR3 statistical model (red) that was used to produce the temporal prior model covariance matrix $\ddot{\mathbf{C}}_{1}$. (a) for the SA coefficient $\ddot{g}_{1}^{0}(t)$ and (b) for the SA coefficient $\ddot{h}_{12}^{12}(t)$. Note the different scales on the *y*-axis. The spectra for the 100p realizations are noisier because they are derived from much shorter timeseries.

coefficients of core field accelerations, derived from geodynamo simulations (see Section 2.2.3), and \mathbf{G}_t the matrix that projects from field accelerations onto the spline basis. $\mathbf{m}_C^T \mathbf{\Lambda}_2 \mathbf{m}_C$ is used to further penalize the acceleration of the core field at the model endpoints. $\mathbf{m}^T \mathbf{\Lambda}_a \mathbf{m}$ collects additional regularization terms used to penalize time-variations in external field parameters and Euler angles involved in the alignment of the vector magnetometer measurements. Further details of the most important terms in the loss function for the core field are given the sub-sections below.

2.2.1. Data misfit

We measure the goodness of fit of the model to the *Swarm* observations via a robust measure of the squared data misfit with

$$\chi^2(\mathbf{m}) = \frac{1}{N} (\mathbf{e}^T \mathbf{W} \mathbf{e}) \tag{5}$$

where **e** is a vector of the residuals $e_i = d_i - [g(\mathbf{m})]_i$ between the observations d_i and the model predictions $[g(\mathbf{m})]_i$ and N is the number of observations. $\mathbf{W} = \mathbf{C}_{\mathbf{e}}^{-1}\mathbf{H}$ is a data weight matrix which is the product of the inverse of the data error covariance matrix $\mathbf{C}_{\mathbf{e}}^{-1}$ (here assumed diagonal) and a diagonal matrix \mathbf{H} containing iteratively updated robust weights derived under the assumption of a long-tailed Huber distribution of residuals (Constable, 1988; Sabaka et al., 2004).

2.2.2. Spatial regularization

Spatial regularization is carried out following Otzen et al. (2024), separately for the core and lithospheric fields, based on the information entropy of their respective radial magnetic fields at their source surfaces, taking into account the a-priori expected field correlations at these surfaces. The spherical harmonic model coefficients are related to the core and lithospheric radial magnetic field evaluated on grids at the core surface (at time t_p) and at the Earth's surface denoted \mathbf{b}_C and \mathbf{b}_L , by

$$\mathbf{b}_{C}(t_{p}) = \mathbf{G}_{C}(t_{p})\mathbf{m}_{C} \quad \text{and} \quad \mathbf{b}_{L} = \mathbf{G}_{L}\mathbf{m}_{L}$$
 (6)

where \mathbf{m}_C denotes the spline coefficients for the time-dependent core field, $\mathbf{G}_C(t_p)$ is a matrix that calculates the radial component of the core field on an approximately equal area grid of 3072 points at the core-mantle boundary at time t_p , from these core field coefficients. \mathbf{m}_L denotes the coefficients for the static lithospheric field, and \mathbf{G}_L is a matrix used to evaluate the radial component of this field on an approximately equal area grid of 49,152 points at Earth's surface. Knowledge of the expected spatial covariance of each field at its source surface is provided in the form of a-priori model covariance matrices \mathbf{C}_C and \mathbf{C}_L , with lower triangular Cholesky factors \mathbf{L}_C and \mathbf{L}_L , which were derived from a large number of field realizations from forward simulations of the core and lithospheric fields (see Otzen et al., 2024, for more

details). These are used to transform $\mathbf{b}_C(t_p)$ and \mathbf{b}_L into decorrelated latent variables $\mathbf{x}_C(t_p)$ and \mathbf{x}_L , see Maisinger et al. (2004) for the importance of accounting for expected correlations when computing the information entropy. The information entropy S for continuous variables that can take both positive and negative values (Gull and Skilling, 1990; Hobson and Lasenby, 1998) is then calculated for both $\mathbf{x}_C(t_p)$ and \mathbf{x}_L using

$$S[\mathbf{x}, \omega] = \sum_{i=1}^{M} \left[\psi_i - 2\omega - x_i \log \left(\frac{\psi_i + x_i}{2\omega} \right) \right]$$
 (7)

where M is the number of grid points on the spherical surface (3072 points for the core field, 49,152 for the lithospheric field), $\psi_i = \sqrt{x_i^2 + 4\omega^2}$, and ω is a 'default' parameter that defines the width of the entropy distribution. For the core field a time-averaged value for the information entropy, S_{tav} is calculated by integrating \mathbf{x}_C over the epochs t_p . Information entropy is a measure of the uncertainty in a random variable \mathbf{x} (Shannon, 1948; Jaynes, 2003). In the geomagnetic context it can be thought of as measuring the number of ways a given distribution of radial field on the source surface can be arranged from elementary flux bundles (Jackson, 2003; Jackson et al., 2007); fields with larger entropy are simpler in that they can be arranged in more ways. We used the same default parameters for the core and lithosphere latent variables as Otzen et al. (2024), $\omega_C = 0.412$ and $\omega_L = 0.422$ respectively, based on the width of the distributions of \mathbf{x}_C and \mathbf{x}_L found from a-priori core field (geodynamo) and lithospheric field simulations.

2.2.3. Temporal regularization

The fourth and fifth terms in the loss function (4) implement the temporal regularization of the core field. The term $\mathbf{m}_C^T \mathbf{\Lambda}_t \mathbf{m}_C$ penalizes departures from a-priori expected temporal covariances of the core field acceleration, as specified in the matrix $\ddot{\mathbf{C}}_t$. $\ddot{\mathbf{C}}_t$ is obtained from statistics computed from geodynamo simulations (the 71p (Aubert and Gillet, 2021) and 100p (Aubert, 2023) geodynamo simulations). To derive the matrix $\ddot{\mathbf{C}}_t$ we fit second time derivative (secular acceleration or SA) coefficients from the geodynamo simulations using a discrete third order auto-regressive (AR3) process of the form (Gillet et al. (2024), equation A.4)

$$\ddot{\mathbf{g}}_{t_{i+3}} + \underline{D}_{2} \ddot{\mathbf{g}}_{t_{i+2}} + \underline{D}_{1} \ddot{\mathbf{g}}_{t_{i+1}} + \underline{D}_{0} \ddot{\mathbf{g}}_{t_{i}} = \underline{B} \boldsymbol{\eta}_{t_{i}}. \tag{8}$$

This involves the geodynamo model SA Gauss coefficient vector \ddot{g} at successive epochs t_i , t_{i+1} , t_{i+2} , t_{i+3} , , and η_{t_i} a multivariate white random noise vector whose covariance matrix is the identity matrix. The elements of the matrices $\underline{\underline{D}}_0$, $\underline{\underline{D}}_1$, $\underline{\underline{D}}_2$ and $\underline{\underline{B}}$ are estimated from geodynamo simulation data using a maximum likelihood approach as described by Gillet et al. (2024) (see their Equations C.8 and A.6). Use of an AR3 process allows the main features of the temporal power

Table 1
Misfit statistics between the Swarm data and the field model constructed in this study. Data is classified as non-polar if collected below ± 55 degrees Quasi-Dipole latitude, and polar if from higher Quasi-Dipole latitudes. Swarm-AC denotes east—west differences between the Alpha and Charlie satellites. Mean and RMS misfits were computed using the robust Huber weights after convergence. N denotes the number of data in each category.

Source	QD lat	N	Misfits for vector and scalar fields								
			B_r		$B_{ heta}$		B_{ϕ}		F		
			Mean (nT)	RMS (nT)	Mean (nT)	RMS (nT)	Mean (nT)	RMS (nT)	Mean (nT)	RMS (nT)	
Swarm-A	non-polar	659,811	0.05	1.65	0.03	2.74	-0.03	2.49			
	polar	171,014							-0.11	3.55	
Swarm-B	non-polar	1, 317, 057	-0.04	1.62	-0.05	2.74	-0.04	2.48			
	polar	341,188							0.05	3.31	
Swarm-C	non-polar	663,556	0.08	1.66	-0.04	2.74	-0.05	2.51			
	polar	171,914							-0.05	3.55	
			Misfits for vector and scalar field differences								
			δB_r		$\delta B_{ heta}$		δB_ϕ		δF		
Source	QD lat	N	Mean (nT)	RMS (nT)	Mean (nT)	RMS (nT)	Mean (nT)	RMS (nT)	Mean (nT)	RMS (nT)	
Swarm-A	non-polar	325,594	0.00	0.24	0.00	0.24	0.00	0.32			
		446,703							0.00	0.17	
	polar	99,399							0.01	0.55	
Swarm-B	non-polar	650,0192	0.00	0.23	0.00	0.24	0.00	0.31			
		446,371							0.00	0.16	
	polar	100,092							0.00	0.49	
Swarm-C	non-polar	327,585	0.00	0.25	0.00	0.25	0.00	0.33			
		449,470							0.00	0.17	
	polar	99,880							0.01	0.56	
Swarm-AC	non-polar	1, 244, 802	0.04	0.45	-0.06	0.52	0.00	0.53			
		1, 704, 255							0.03	0.38	
	polar	385,358							0.06	0.43	

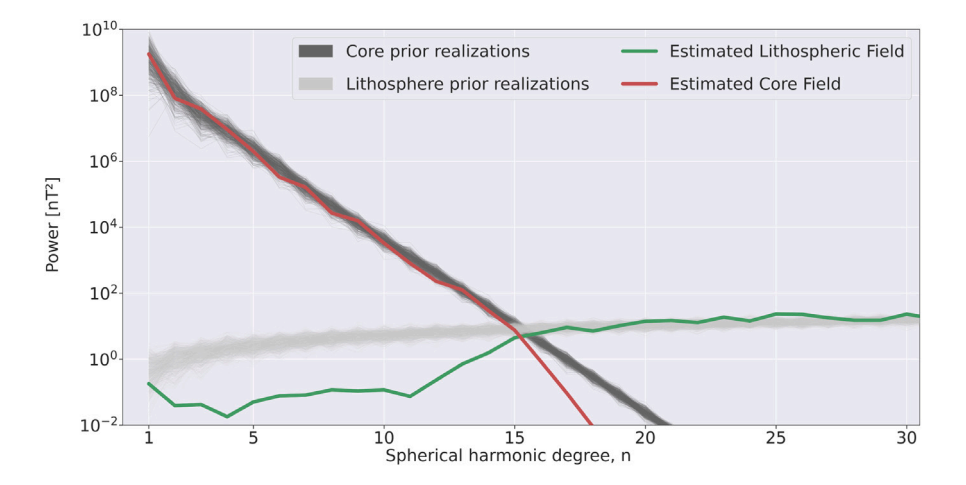


Fig. 2. Spherical harmonic power spectra showing the mean squared vector field strength integrated over Earth's surface as a function of spherical harmonic degree in 2019.5. Thick lines show the estimated core and lithospheric fields. Thin lines show example realizations of the a-prior core (dark grey) and lithospheric (light grey) fields.

spectra of the SA coefficients to be captured, in particular being rather flat at low frequencies and gradually transitioning to a step decay at high frequencies (modelled here as an f^{-6} decay since we employ AR3 processes, but in reality even steeper than this). For other examples of the use of AR3 processes in geomagnetism see Sadhasivan and Constable (2022) and Gillet et al. (2024). Comparisons of temporal spectra for example SA coefficients $(\ddot{g}_1^0(t)$ and $\ddot{h}_{12}^{12}(t))$, for periods between 1 and 100 years, from the considered geodynamo simulations (black and grey lines) together with realizations of the fitted AR3 process (red) are shown in Fig. 1. The AR3 models reproduce the nearly flat SA spectra found in the 71p dynamo at low frequencies (periods longer a few decades) and also the steep slope at periods less than 5 years found in the 100p dynamo realizations. The AR3 model generally contains more power than the 71p dynamo, except at the very highest frequencies.

The AR3 spectra (red lines) are characteristic of the temporal prior information implemented in our inversion scheme.

Once the coefficients of the multivariate AR3 process (8) are derived we integrate the AR3 stochastic equation forward in time using an Euler–Maruyama scheme (Gillet et al., 2024) with a timestep of 0.2 years. In this way we obtain long timeseries of the SA coefficients that reproduce the relevant statistics of the shorter geodynamo simulation runs. From these long AR3 model time series we derive a well-conditioned empirical covariance matrix containing information on the covariances between all SA coefficients up to our spherical harmonic truncation degree 22 and considering time separations up to our model length of 11 years in steps of 0.2 years. In \ddot{C}_t we retain only the temporal covariances of the SA coefficients, and not the cross-covariances between SA coefficients of different degree or order, which are also estimated but may be more affected by the specifics of the

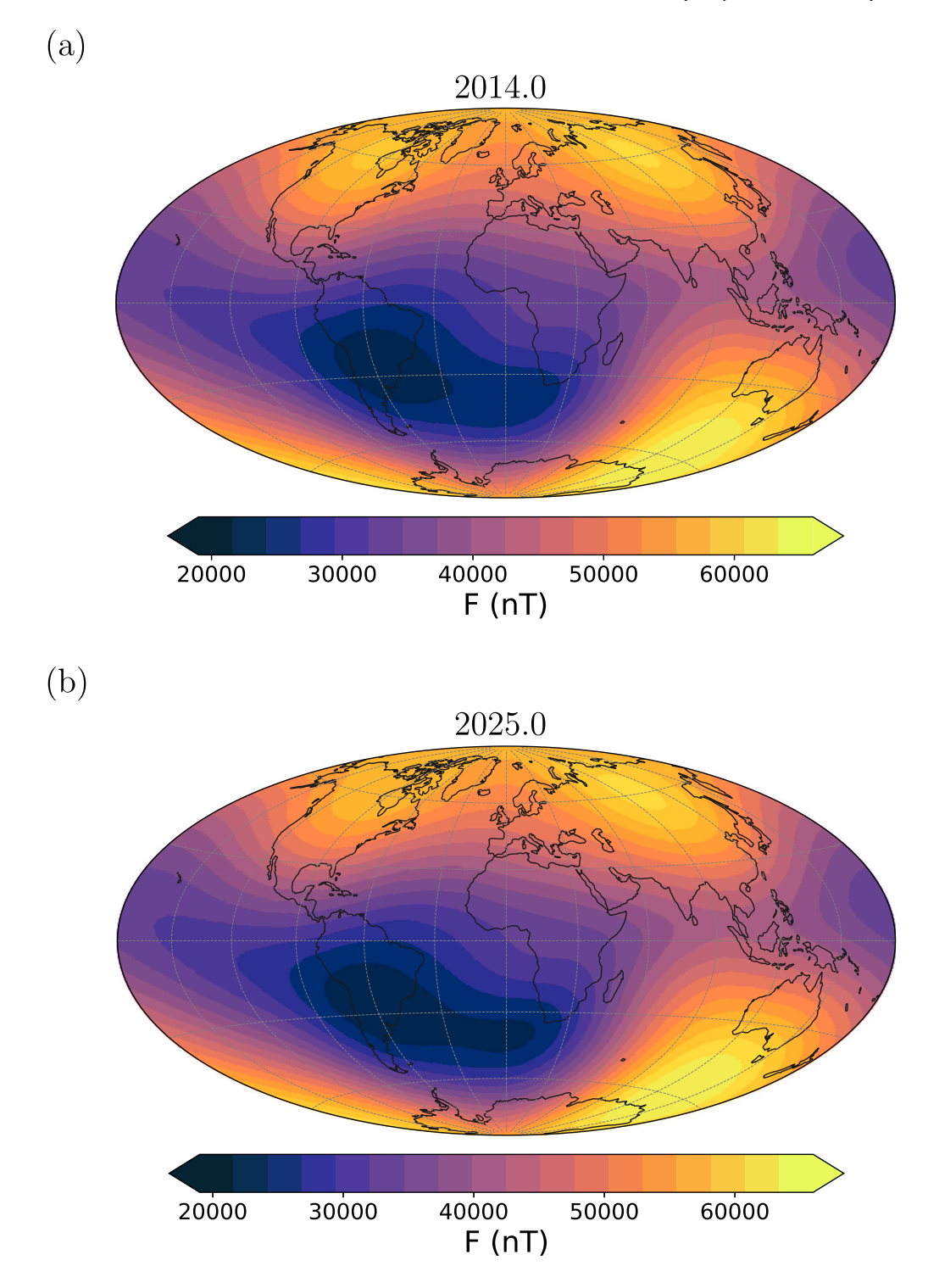


Fig. 3. Magnetic field Intensity (F) at Earth's surface in Epoch 2014.0 (top) and Epoch 2025.0 (bottom). Presented in Hammer projection. Units are nanoTesla (nT). From the estimated Swarm-based core field model up to spherical harmonic degree 22.

geodynamo simulation setup. Our approach includes information on the different temporal behaviour expected for each spherical harmonic coefficient of the SA, for example treating sectoral terms differently from the zonal terms. This seems reasonable as higher amplitude SA variations are expected for sectorial coefficients due to the arrival of QGMC waves at the CMB (see Aubert et al. (2022), Gerick and Livermore (2024)), while more gradual changes are expected for zonal terms. Finally we compute $\ddot{\mathbf{C}}_t^{-1}$, making use of Cholesky decomposition,

and then project onto the sixth order spline basis of our core field model to obtain the temporal regularization matrix $\mathbf{\Lambda}_t = \mathbf{G}_t^T \ddot{\mathbf{C}}_t^{-1} \mathbf{G}_t$ using an appropriate spline collocation matrix \mathbf{G}_t .

An additional core field regularization term $\mathbf{m}_C^T \mathbf{\Lambda}_2 \mathbf{m}_C$ measures the squared acceleration of the radial field at the endpoints of the model. As in the CHAOS model series this is used as an extra control on the SA at the model endpoints where there is less data constraint.

3. Observations from the Swarm satellite trio

In this study we used only data from the *Swarm* mission, in the form of vector field measurements in the non-polar region (Quasi-dipole latitudes below 55 degrees) and scalar field intensity measurements at higher latitudes, as well as along-track differences for each of the three satellites and east—west field differences between the *Swarm* Alpha and Charlie satellites. We used the operational *Swarm* data product SW_OPER_MAGX_LR_1B, taking the latest available versions, 0602 to 0605, at 15 s sampling, between 2014.0 and 2025.0. We used a 30 s sampling of data from the *Swarm* Bravo satellite and a 60 s sampling from *Swarm* Alpha and Charlie, since Alpha and Charlie fly close together. Only night-side data is used since we do not seek to co-estimate the ionospheric field. The same geomagnetic quiet-time criteria used in deriving the CHAOS-7 field model (Finlay et al., 2020) are adopted here for the vector field and scalar intensity observations.

For the along-track and east—west field differences, following Olsen et al. (2017), we used a relaxed geomagnetic quiet time selection criteria. This is permitted since the differencing acts to remove much of the large-scale external field disturbance. We used scalar field gradients at all latitudes, not only in the polar region.

In all, after data selection, we considered 2,640,424 vector field triples, 684,116 scalar intensity measurements, 2,548,173 vector field triple differences, and 3,731,528 scalar field differences.

4. Results

4.1. Fit to Swarm data and spatial spectra

In Table 1 we present misfit statistics quantifying differences between predictions of the field model described above and the magnetic field measurements collected by the *Swarm* satellites. We find our model fits the considered (night-side, geomagnetically quiet) vector field data at non-polar latitudes to within 1.66 nT in B_r , 2.74 nT in B_θ and 2.51 nT in B_ϕ while similar along-track field differences were fit to within 0.25 nT in B_r , 0.25 nT in B_θ and 0.33 nT in B_ϕ . East—west field differences between *Swarm* Alpha and Charlie were fit to within 0.45 nT in B_r , 0.52 nT in B_θ and 0.53 nT in B_ϕ . Mean residuals were found to be small, of order 0.1 nT or less in all components. Overall we find the derived field model is thus an acceptable representation of the *Swarm* data.

Fig. 2 shows the degree variance or Lowes-Mauersberger spatial power spectra of the estimated core and lithospheric field models (red and green lines respectively) at Earth's surface. Also shown for reference are example spectra of a-priori realizations of core and lithospheric fields (dark and light grey lines respectively) constructed using the spatial correlation information employed in the entropy regularization. Note the decrease in power above degree 15 for the estimated core field and below degree 15 for the estimated lithospheric field where the constraints on these field components from the observations are weak. The estimated (a-posteriori mean) models at these degrees return towards the zero mean of the a-priori models. Spectra of a-posteriori realizations (not shown) agree closely with the core and lithospheric a-priori realizations at low degrees for the lithospheric field and high degrees for the core field. For further discussion of the chosen priors and the interpretation of the a-posteriori realizations see Otzen et al. (2024). We next proceed to present results as to how the field has changed between 2014.0 and 2025.0.

4.2. Field intensity changes at the Earth's surface

4.2.1. The South Atlantic anomaly weak field region

In Fig. 3 we present the intensity (F) of Earth's magnetic field at Earth's mean spherical surface in Epochs 2014.0 and 2025.0. The weak field region in the South Atlantic, shown by the darkest colours, has clearly expanded over the 11 years of observation by *Swarm*. This is

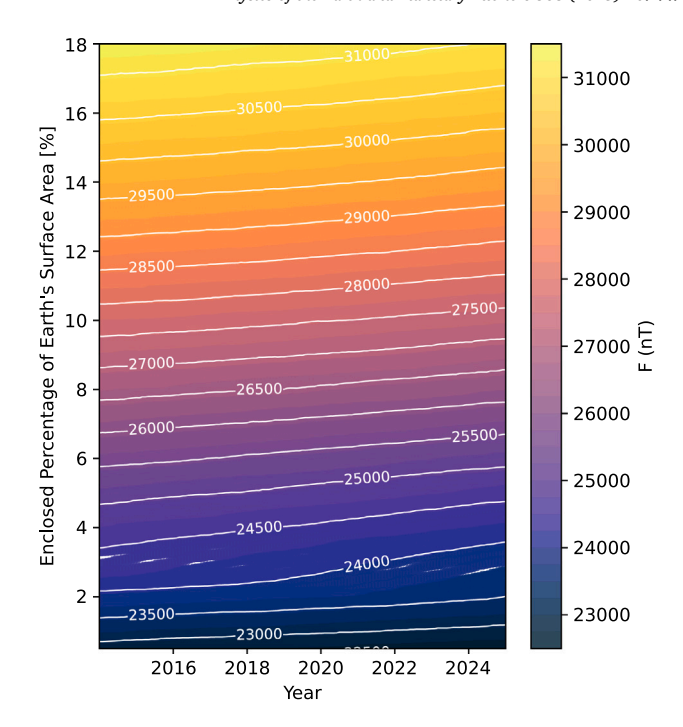


Fig. 4. Evolution of the South Atlantic weak field region in terms of the area contained within contours of magnetic field Intensity (F) at Earth's surface between 2014.0 and 2025.0. From the estimated *Swarm*-based core field up to spherical harmonic degree 22.

in agreement with earlier studies of the SAA with *Swarm* data e.g. Campuzano et al. (2021). The most notable change is the field weakening to the south-west of South Africa. Previous studies (Finlay et al., 2020; Rother et al., 2021) highlighted the appearance of a secondary minimum of the field intensity in this region; with the contour intervals adopted here this secondary minimum has expanded and merged with primary field intensity minimum that is located near South America, which has also expanded since 2014.

To avoid any ambiguity related to the choice of specific field intensity contours in Fig. 3, in Fig. 4 we present in a more continuous manner how the area contained within field intensity contours has evolved between 2014.0 and 2025.0 in the South Atlantic region. By choosing a specific colour and following it with time one can see how the area contained within a specific contour (measured as a percentage of Earth's mean spherical surface area) has changed. Note the colour scale used in Fig. 4 is altered compared with Fig. 3 as we here focus only on the weakest field values below 32,000 nT. The white contours show the intensity values in steps of 500 nT in order to aid visibility. The area contained within all the considered weak field contours, up to 32,000 nT, has steadily increased from 2014.0 to 2025.0. This demonstrates that the observed expansion of the South Atlantic weak field anomaly is not related to the choice of specific contours. A larger increase in the enclosed area is seen for contours around $24,000\,\mathrm{nT}$ which is related to the development of the secondary minimum in field intensity south-west of Africa. The area enclosed within the 24,0000, 26,000, 28,000 and 30,000 nT contours increased in size between 2014.0 and 2025.0 by 1.41%, 0.91%, 0.88% and 0.97% of Earth's (mean spherical) surface area respectively. It is instructive to compare these changes in area to the area of Greenland which is 0.42% of Earth's surface area.

4.2.2. Intensity maxima in the polar regions

In Fig. 5 we next document the field intensity at Earth's surface in the northern polar region in 2014.0 and 2025.0. In this part of the

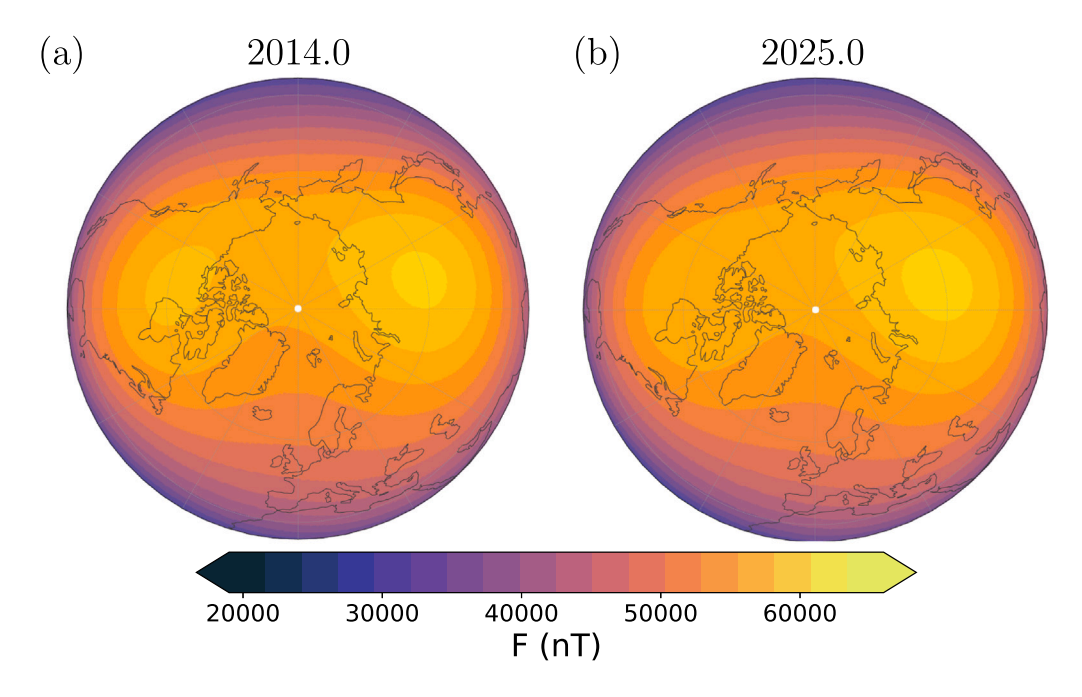


Fig. 5. Magnetic Field Intensity (F) at Earth's surface in the northern polar region (a) in Epoch 2014.0 and (b) in Epoch 2025.0. Units are nanoTesla (nT) Presented in an Azimuthal Nearside Perspective projection. From the estimated Swarm-based core field up to spherical harmonic degree 22.

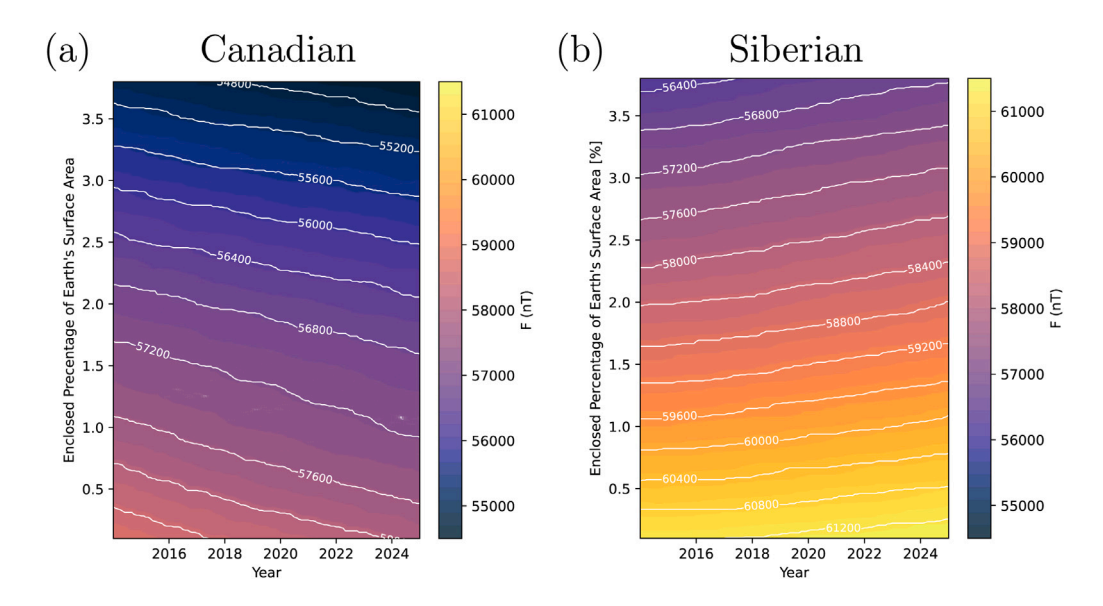


Fig. 6. Evolution of the strong field maxima in the Northern polar region in terms of the area contained within contours of magnetic field Intensity (F) at Earth's surface between 2014.0 and 2025.0. (a) For the Canadian field maximum and (b) for the Siberian field maximum. From the estimated *Swarm*-based core field up to spherical harmonic degree 22.

globe there has been significant evolution of the strongest field features, with the intensity decreasing in Canada, and increasing in Siberia (see also Livermore et al. (2020)). This is clearly evident in Fig. 6 with the brightest gold coloured regions, that indicate the strongest field intensities, vanishing in Canada while similar strong field regions in Siberia have increased in area.

These changes in the northern hemisphere strong field regions between 2014.0 and 2025.0 are further quantified in Fig. 6 which presents the evolution in the area (again given as a percentage of the area of Earth's surface) contained within contours of field intensity greater than 54,000 nT between 2014.0 and 2025.0, in Canada and Siberia

respectively, separated by considering longitudes in the western and eastern hemispheres respectively. Fig. 6 shows that the area covered by contours of the strongest field has steadily decreased in Canada and steadily increased in Siberia over the past 11 years; the colours indicating the magnitude of the field strength are the same in the two subplots. For example the area enclosed within the 55,000 nT and 57,000 nT contours in Canada have decreased by 0.41% and 0.65% of Earth's (mean spherical) surface area respectively while the area enclosed within the same contours in Siberia has increased by 0.42% and 0.42% respectively and 0.36% for the 59,000 nT contour. At the same time, the maximum field strength (calculated considering the core

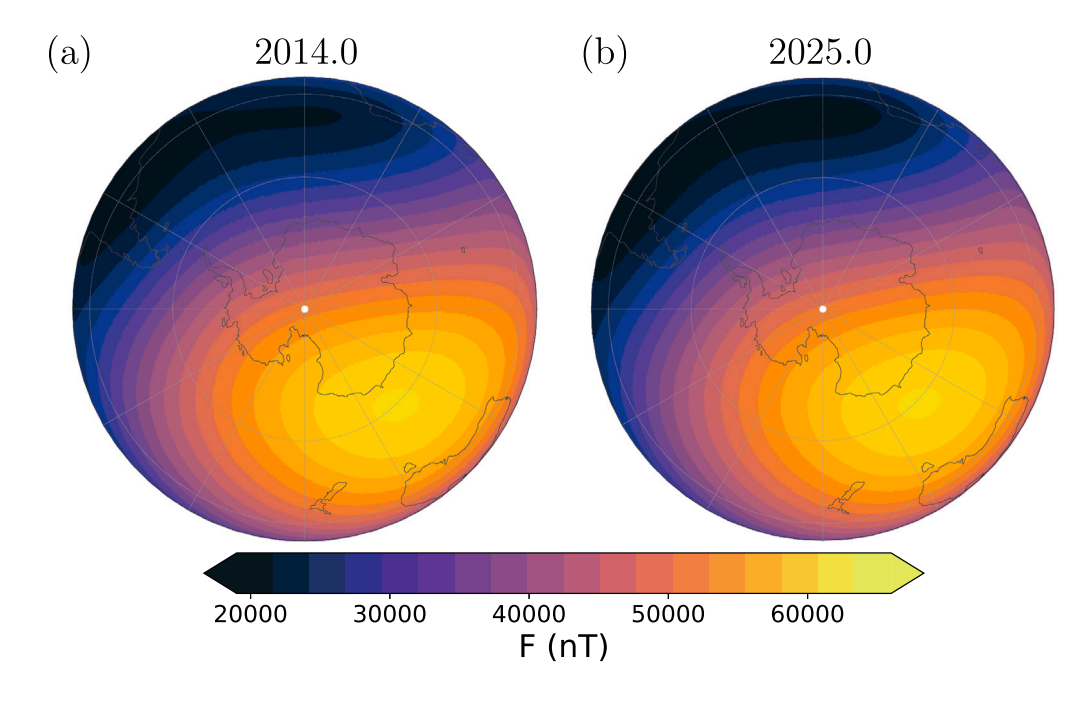


Fig. 7. Magnetic Field Intensity (F) at Earth's surface in the Southern polar region (a) in Epoch 2014.0 and (b) in Epoch 2025.0. Units are nanoTesla (nT). Presented in an Azimuthal Nearside Perspective projection. From the estimated Swarm-based core field up to spherical harmonic degree 22.

field up to degree 22) in Canada decreased by 1.4% from 58,832 nT to 58,031 nT between 2014.0 and 2025.0 while over the same period in Siberia the maximum field strength increased by 0.5% from 61,359 nT to 61,619 nT.

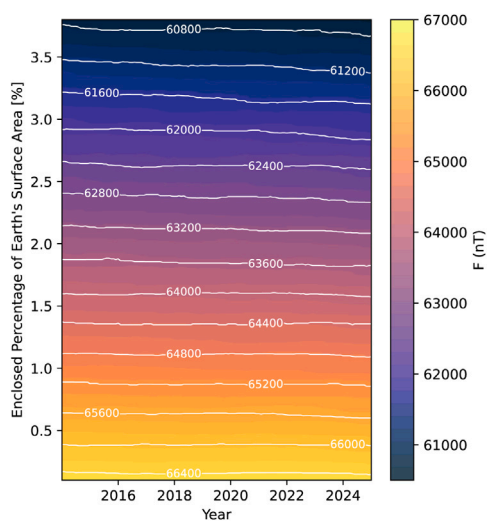


Fig. 8. Evolution of the strong field maximum in the Southern polar region in terms of the area contained within contours of magnetic field Intensity (F) at Earth's surface between 2014.0 and 2025.0. From the estimated *Swarm*-based core field.

In Fig. 7 we next examine the field intensity in 2014.0 and 2025.0 in the Southern polar region. Here there is only a single maximum in the field intensity between Australia and Antarctica. It is at similar longitude as the Siberia field maxima but covers a larger region (see Fig. 3). Fig. 7 suggests that, in contrast to the situation in the northern hemisphere, the change in the southern field maxima between 2014.0 and 2025.0 has been relatively minor. This is confirmed in Fig. 8 which shows the area enclosed by contours of highest field intensity in the Southern hemisphere has only slightly decreased between 2014.0 and

2025.0; the areas enclosed by the 62,000 nT, 64,000 nT and 66,000 nT contours have decreased by 0.1%, 0.03% and 0.01% of Earth's surface area between 2014.0 and 2025.0, much smaller than the changes seen in the northern hemisphere. The maximum field intensity in the southern polar region (considering up to degree 22 of the core field) decreased by 0.05% from 66,678 nT in 2014.0 to 66,641 nT in 2025.0.

4.3. Radial field evolution at the core-mantle boundary

4.3.1. Radial field and Secular Variation (SV)

The evolution of the surface field features described above ultimately result from magnetohydrodynamic processes taking place within Earth's core. Our field estimation scheme is specifically designed for study of the core field, with spatial and temporal regularizations that are motivated by the processes expected in the core (Otzen et al., 2024; Gillet et al., 2024). We therefore now proceed to examine the core field changes captured by our model at the core-mantle boundary.

In Fig. 9 we first present the core-mantle boundary radial magnetic field in 2014.0 and 2025.0, together with the average field change (or Secular Variation, SV) over these eleven years up to spherical harmonic degree 13. Degree 13 is the conventional choice for the cut-off spherical harmonic degree when examining the field at the core-mantle boundary, as higher degrees are usually contaminated by the lithospheric field signal. We find the radial field up to degree 13 has maintained a very similar morphology between 2014.0 and 2025.0, the most obvious change being the movement of strong positive field features westward under Africa and the westward movement and intensification of the negative (reversed flux) patch under Southwestern Africa. In the northern polar region a strong field concentration under Siberia has moved westward and southward, while a strong field concentration under Alaska has moved rapidly westwards and become more clearly separated from another strong field concentration under Canada.

When interpreting CMB SV patterns such as Fig. 9 c it is useful to remember that, in the simple case of a steady and uniform background field, a drifting field feature of constant amplitude will produce a pair of oppositely signed SV features one either side, one in the region it

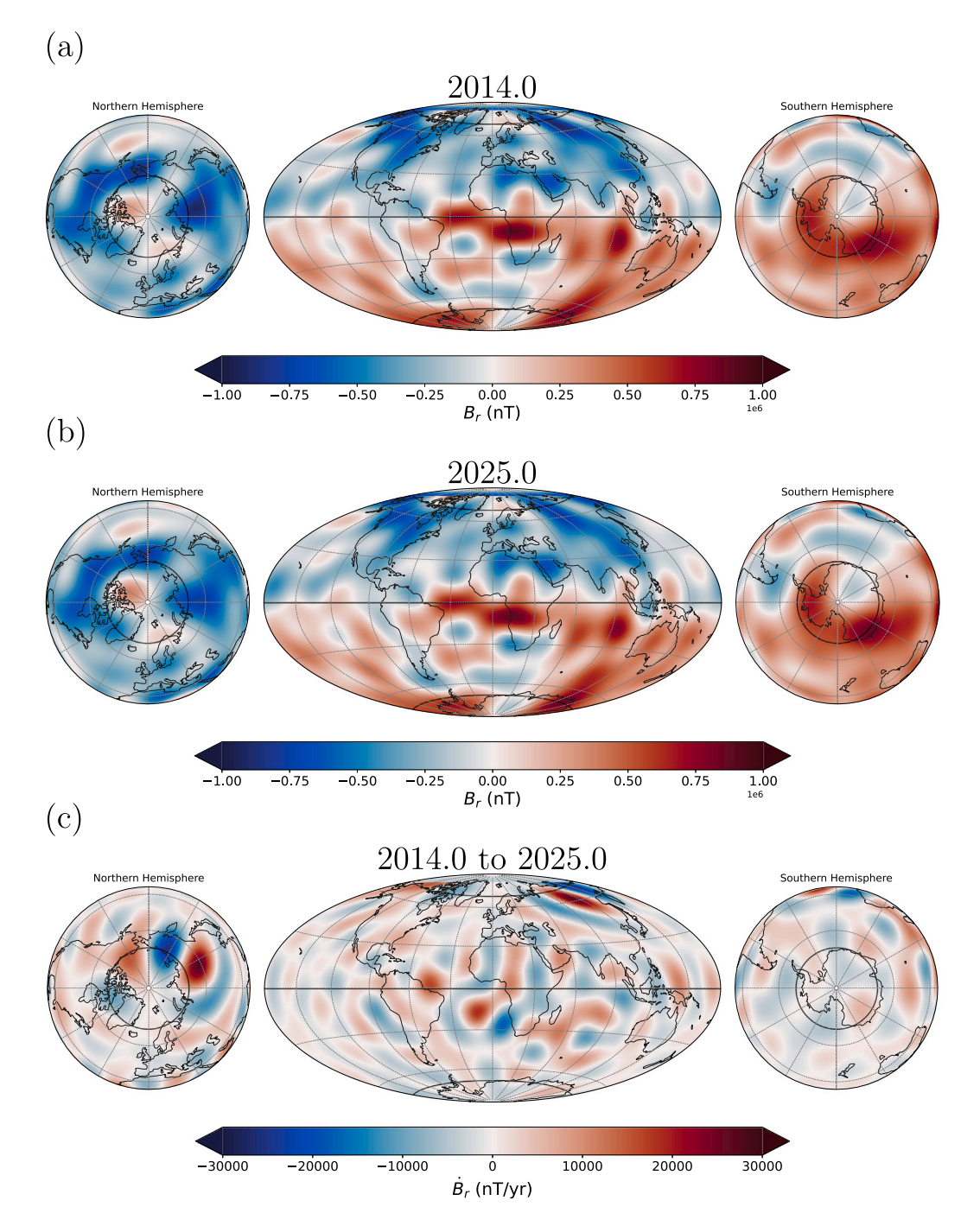


Fig. 9. Radial component of Earth's magnetic field at the core-mantle boundary up to spherical harmonic degree 13. (a) In Epoch 2014.0, (b) In Epoch 2025.0 and (c) Change between 2014.0 and 2025.0 expressed in nT/yr. From the estimated *Swarm*-based core field model. Thick black lines mark the geographic equator and the intersections of the northern and southern inner core tangent cylinders with the core-mantle boundary.

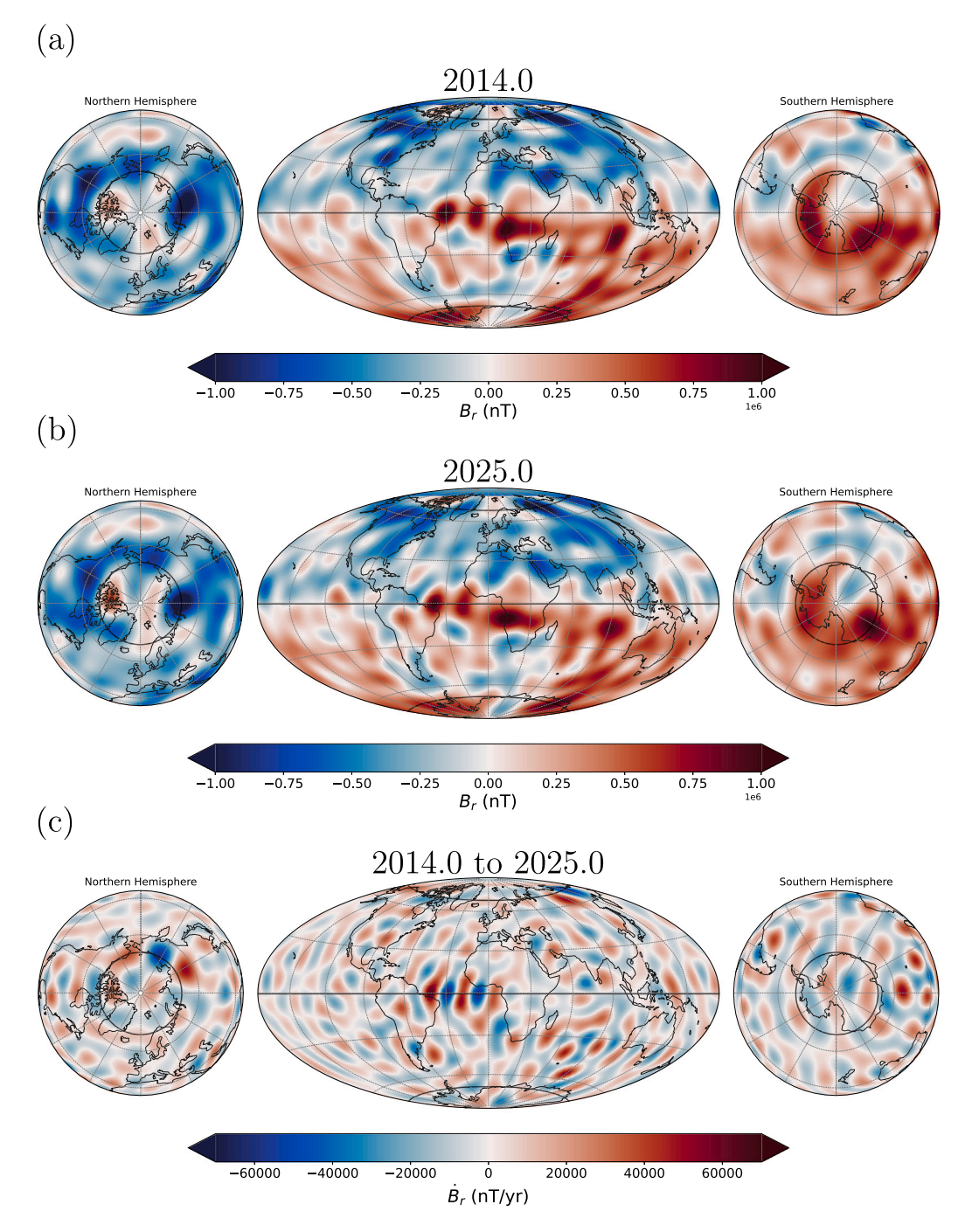


Fig. 10. Radial component of Earth's magnetic field at the core-mantle boundary up to spherical harmonic degree 20. (a) In Epoch 2014.0, (b) In Epoch 2025.0 and (c) Change between 2014.0 and 2025.0 expressed in nT/yr. From the estimated *Swarm*-based core field model. Thick black lines mark the geographic equator and the intersections of the northern and southern inner core tangent cylinders with the core-mantle boundary.

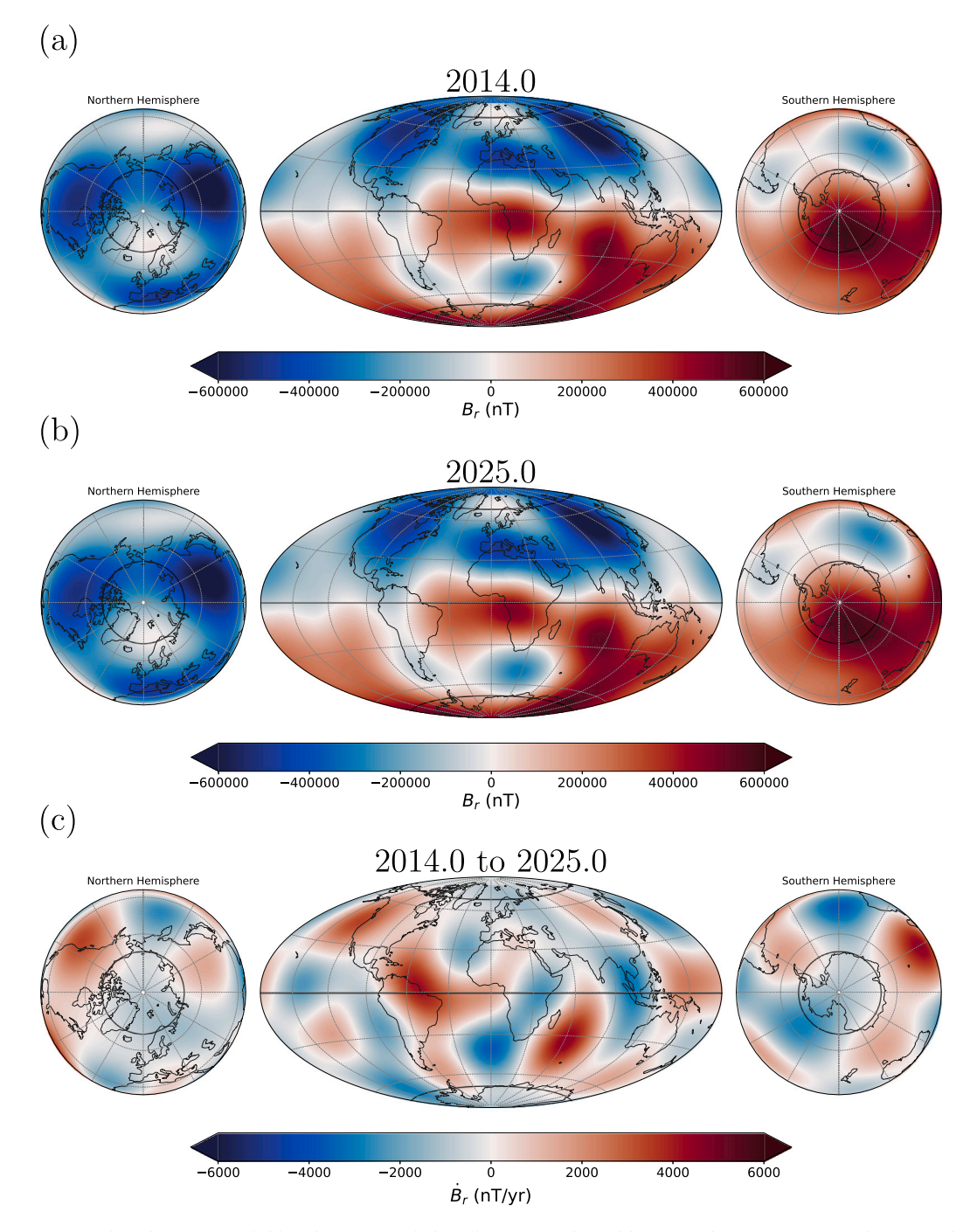


Fig. 11. Radial component of Earth's magnetic field at the core-mantle boundary up to spherical harmonic degree 6. (a) In Epoch 2014.0, (b) In Epoch 2025.0 and (c) Change between 2014.0 and 2025.0 expressed in nT/yr. From the estimated *Swarm*-based core field model. Thick black lines mark the geographic equator and the intersections of the northern and southern inner core tangent cylinders with the core-mantle boundary.

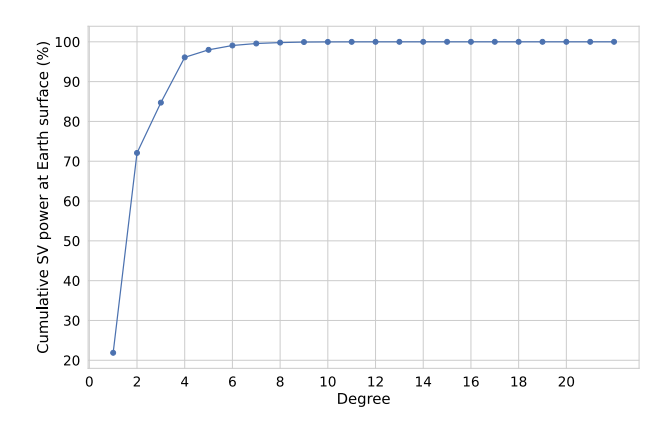


Fig. 12. Cumulative SV power at Earth's surface as a function of spherical harmonic degree, shown as a percentage, and averaged over 2014.0 to 2025.0. This quantifies how much of the mean squared vector field SV is captured as the spherical harmonic degree increases. 99.1% of the SV power is already captured when degrees up to 6 are included.

moves into and the other in the region it moves away. Stationary but intensifying/weakening field features on the other hand will produce SV features that are positively and respectively negatively correlated with the locations of the field features (Amit et al., 2021).

Since we explicitly attempt to co-estimate the lithospheric field, we can also examine the estimated core-mantle boundary radial field to higher degree, this is shown in Fig. 10 where the spherical harmonic truncation degree was set to 20. We find that the reversed flux feature under the central south Atlantic (located near longitude 25 degrees West and latitude 50 degrees South in 2014.0) has moved noticeably eastward by 2025.0 so that the reversed flux features under southern America are now more obviously separated from those located under southern Africa and extending southwards.

In Fig. 11 we present a much simpler picture of the evolution the core-surface radial field, only up to spherical harmonic degree 6, note the change in scale in this case. Fig. 12, which shows the cumulative mean squared secular variation of the vector field at Earth's surface as a function of spherical harmonic degree, demonstrates that when considering spherical harmonic degrees only up to 6, 99.1% of the power of surface field SV is already captured. This motivates us to examine changes only up to degree 6 at the core-mantle boundary, in an effort to see which CMB field changes are responsible for the changes seen in the surface field. We find that the large-scale part of the reversed flux feature located underneath and to the south of Africa has overall moved westward while that under south America has moved slightly westwards and equatorward. The radial field concentration under Canada has decreased in size and strength while that under Siberia has expanded.

4.3.2. Radial field Secular Acceleration (SA)

We now finally consider the estimated radial field secular acceleration (SA) at the core-mantle boundary, up to spherical harmonic degree 9. Fig. 13 first presents the SA time-averaged over 2014.0 to 2025.0. Prominent regions of SA are seen under the Bering strait, under the eastern edge of South America below the equator and also under Indonesia and the western Pacific. The latter oppositely signed features seem to be due an accelerating eastward movement of radial field concentrations under Indonesia and the western Pacific in Figs. 9 and 10 that agrees with recent inferences of eastward flow development at low latitudes under the western Pacific (Whaler et al., 2022; Ropp and Lesur, 2023; Rogers et al., 2025).

To document the dynamic nature of the CMB SA, in Fig. 14 we present maps of the radial SA at the CMB, up to spherical harmonic degree 9, in 2015.0, 2018.0, 2021.0 and 2024.0, that is in steps of 3 years but avoiding the first and last years of the model when the acceleration is affected by end-effects. The radial SA in each epoch is much larger than the time-averaged SA from the previous Figure, and is found to be especially dynamic at low latitudes. Some interesting patterns are evident, for example in 2015.0 and 2021.0 the acceleration patterns in the equatorial Pacific are rather similar, while opposite signed acceleration is found in this region in 2018.0. This agrees with previous studies that have suggested the presence of rapid (interannual) oscillatory disturbances in the low latitude CMB SA (Chulliat and Maus, 2014; Finlay et al., 2015).

Further insights into the evolution of CMB radial field SA features in the east-west direction are provided by the time-longitude plots in Fig. 15. The largest amplitude SA is seen at the equator where there is evidence for westward propagating features in the central Pacific between 2017 and 2020. Similar time-longitude plots are also presented at the latitudes where the northern and southern inner core tangent cylinders intersect the CMB. Here the SA patterns are of lower azimuthal order and there is evidence for westward drifts of the SA patterns near the northern hemisphere tangent cylinder between 2015 and 2021, and faster drift of SA features near the southern hemisphere tangent cylinder between 2020 and 2023. The SA near the tangent cylinder is clearly not symmetric between the two hemispheres, in agreement with earlier studies that concluded the underlying core flows were also asymmetric between the northern and southern tangent cylinders (Gillet et al., 2019). Further analysis of these drifting SA features is needed, we postpone this to future studies considering longer time series.

5. Discussion and conclusions

The results presented above illustrate the detailed picture of Earth's evolving core-generated magnetic field that has been provided over the past 11 years by the *Swarm* satellites. The restriction imposed here to the past eleven years, by considering only observations from the *Swarm* satellites, is however somewhat artificial. Earlier magnetic survey satellite missions have provided comparable information, albeit for shorter periods. In Table 2 we collect similar diagnostics on the SAA and the northern and southern hemisphere field maxima over the past 55 years, considering the epochs 1970.0, 1980.0 and 2002.0 when the POGO, Magsat, and the Oersted and CHAMP missions, respectively, were in operation. We computed similar diagnostics as those presented above in Section 4.2 for the pre-*Swarm* epochs using the CM4 model (Sabaka et al., 2004) which conveniently covers all these epochs, has a focus on satellite measurements, and also co-estimated an external field.

From Table 2, concerning the SAA, we find that the growth of the weak field region observed by *Swarm* continues the trend seen by earlier missions. More surprising is the relatively rapid shrinkage of the Canadian strong field region. This had already begun in 2002 but little change was observed between the earlier epochs of 1970 and 1980. The growth of the corresponding Siberian strong field feature follows a similar pattern, changing little at the earlier epochs and with the largest

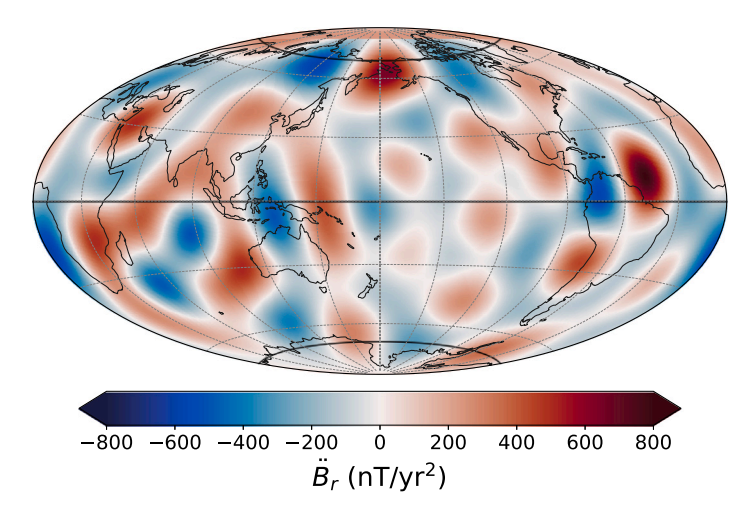


Fig. 13. Time-average of the second time derivative (or Secular Acceleration) of the radial component of Earth's magnetic field at the core-mantle boundary, averaged over 2011.0 to 2025.0. Units are nT/yr^{-2} . From the estimated *Swarm*-based core field up to spherical harmonic degree 9.

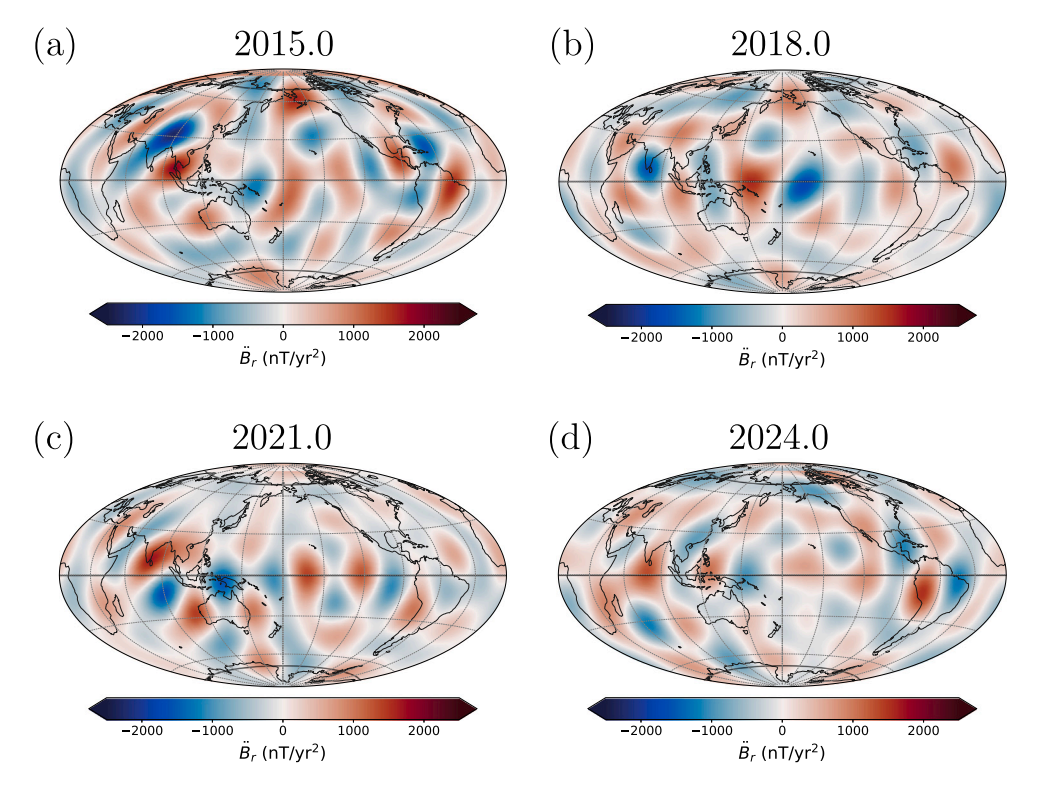


Fig. 14. Time sequence of second time derivative (or Secular Acceleration) of the radial component of Earth's magnetic field at the core-mantle boundary. (a) In Epoch 2015.0, (b) In Epoch 2018.0, (c) In Epoch 2021.0 and (d) In Epoch 2024.0. Units are nT/yr⁻². From the estimated *Swarm*-based core field up to spherical harmonic degree 9.

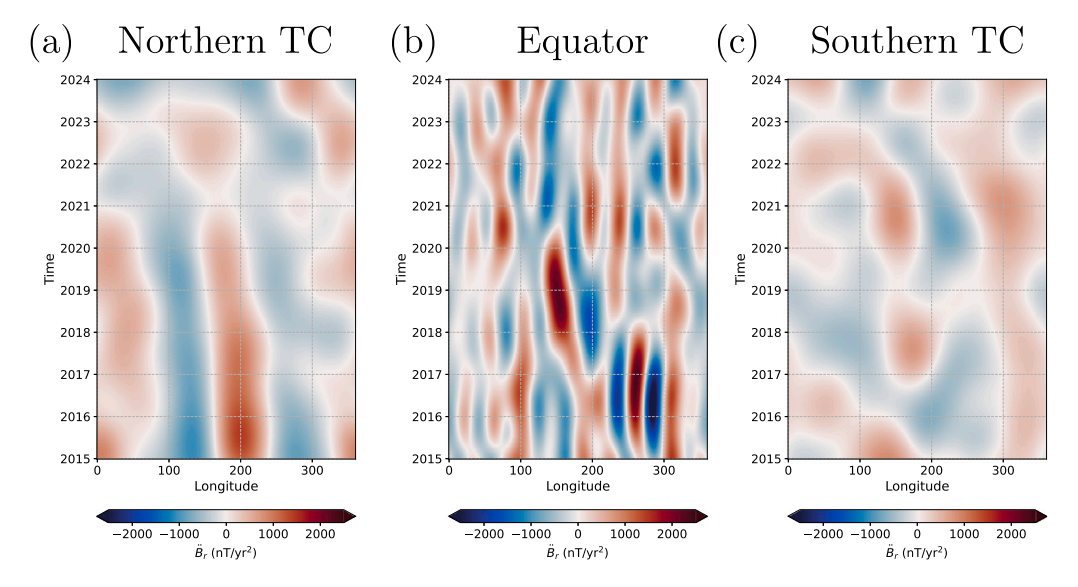


Fig. 15. Time-longitude plots of the second time derivative (or Secular Acceleration) of the radial component of Earth's magnetic field at the core-mantle boundary, spanning 2015.0 to 2024.0 and all longitudes. (a) At the northern hemisphere inner core tangent cylinder (latitude 69.6 degrees), (b) At the equator (c) At the southern hemisphere inner core tangent cylinder (latitude –69.6 degrees) Units are nT/yr⁻². From the estimated *Swarm*-based core field up to spherical harmonic degree 9.

rate of change observed between 2014.0 and 2025.0. This suggests that the diminishing of the Canadian field maxima and the growth of the Siberia maxima are linked, consistent with the elongation and splitting of north American CMB flux lobe discussed by Livermore et al. (2020). Concerning the southern hemisphere field maxima, Table 2 shows that this had earlier decreased in size more rapidly (see, for example Kakad and Kakad (2022)): the minor changes observed over the past 11 years suggest the decline in the strength of this Southern hemisphere field maximum has recently slowed.

When assessing the results reported above for the evolution of the core field, a natural question is what error estimates should we associated with our core field models. It is possible to derive formal model error estimates as part of the field modelling. For our core field models, we follow Otzen et al. (2024) and generate an ensemble of a-posteriori models, then compute the rms deviation of these models from the aposteriori mean model (the model we have analysed in depth above), in terms of their predictions for the field intensity *F* at Earth's surface. Finally we average these rms deviations over a grid at the Earth surface. This procedure results in an estimate of the formal posterior model error in F at Earth's surface of 2.3 nT, much smaller than the changes in F at Earth's surface between 2014 and 2025 (up to 1300 nT, with the rms change being 463 nT) that we have interpreted here. It should be remembered that this formal error is a lower bound on the true error which will also involve errors due to leakage from unmodelled ionospheric, Earth-induced and oceanic fields which may add up to several nanoTesla. Further work on better quantifying the errors in core field models, especially at the CMB, is needed for applications such as core flow modelling and data assimilation using geodynamo simulations.

Regarding the origin of the field intensity changes currently taking place in the northern polar and southern Atlantic regions, two classes of underlying core processes can be envisaged (i) Advection and stretching of the magnetic field by the core flow, and (ii) Expulsion of magnetic flux involving upwelling core flows and magnetic diffusion effects. Troyano et al. (2020) suggest intensity variation rates at Earth's surface due to flux expulsion of 0.01 to 1 $\mu T/yr$ are plausible, while in our field model we find intensity rates of change of up to 0.2 $\mu T/yr$. In terms of the rates involved, flux expulsion is therefore a possibility. The patterns of CMB radial field change in the northern polar region

do however seem to be more readily explained by field advection and stretching (Gillet et al., 2019; Livermore et al., 2020). Regarding the South Atlantic region, differential westward advection and related gathering/dispersal of CMB field features is certainly responsible for part of the observed changes (Finlay et al., 2020). The presence of nearby reversed and normal flux features in the South Atlantic CMB field (see Figs. 9–11) do however seem to hint that magnetic flux expulsion may also be operating in this area (Bloxham, 1986). Comparisons of satellite-based core field models, with episodes of dynamic flux expulsion identified in geodynamo simulations (which typically involve the development of normal-reversed flux pairs) are needed to clarify the role of flux expulsion.

We emphasized above that the field changes observed at Earth's surface must necessarily stem from changes in the large-scale part of the core-mantle boundary field (below degree 6). This is an inevitable consequence of the rather long distance (2900 km) between the Earth's surface and the sources in the core, and the geometric attenuation of a potential field with distance from the source (Gubbins and Roberts, 1983; Backus et al., 1996). If one wishes to explain changes in the field at Earth's surface, the important question is then what controls the large-scale (spatially-averaged) properties of the core-mantle boundary field and its evolution. Recent geodynamo studies (Aubert et al., 2017; Aubert, 2019) have shown that the evolution of the core field on decadal timescales is rather insensitive to the small-scale details of the core flow, with the large-scale buoyancy field (Aubert, 2015, 2020), and core-mantle coupling torques (Pichon et al., 2016; Schwaiger et al., 2024), controlling much of the secular variation. Large-scale hydromagnetic waves may also contribute to the picture, especially when considering transient dynamics (Istas et al., 2023; Gillet et al., 2024; Li et al., 2024). Whether or not it could be feasible to construct better 'effective field' theories for the largest (observable) scales, in which the large-scale dynamics are modelled deterministically while the small-scale details are treated stochastically and integrated over in an appropriate fashion, is unclear. Further efforts in this direction would certainly be of interest.

There is no doubt that the relative short timespan of the presently available satellite magnetic field measurements is a major limitation. The *Swarm* mission has been crucial in extending this record over the past decade and it will remain indispensible for the foreseeable future.

Table 2
Areas within field intensity contours at times of magnetic field survey satellite missions. Using the CM4 model (Sabaka et al., 2004) for Epochs 1970.0, 1980.0 and 2002.0 and the Swarm-based model constructed here for Epochs 2014.0 and 2025.0. Areas are given as a percentage of Earth's mean spherical surface area.

Feature	Contour level F (nT)	POGO 1970.0 (%)	Magsat 1980.0 (%)	Oer/CHAMP 2002.0 (%)	Swarm 2014.0 (%)	Swarm 2025.0 (%)
SAA	24,000	0.21	0.56	1.52	2.16	3.57
	26,000	2.72	3.31	5.71	6.74	7.65
	28,000	5.90	7.16	9.65	10.47	11.35
Canada	55,000 57,000 59,000	4.94 3.21 1.47	4.84 3.16 1.40	4.17 2.34 0.58	3.78 1.96	3.37 1.31
Siberian	55,000	4.32	4.32	4.44	4.73	5.15
	57,000	2.92	2.90	2.93	3.21	3.63
	59,000	1.42	1.40	1.38	1.48	1.84
S. Polar	62,000	4.09	3.71	3.16	2.93	2.83
	64,000	2.63	2.25	1.77	1.60	1.57
	66,000	1.20	0.88	0.48	0.39	0.38

Although there is now a new complementary source of absolute magnetic measurements at mid and low latitudes from the Chinese MSS-1 satellite (Zhang, 2023; Jiang et al., 2024), the exciting prospect of ESA's upcoming NanoMagsat mission (Hulot et al., 2018; Deconinck et al., 2025), and numerous platform magnetometers that can be calibrated to provide improved spatial coverage (Olsen et al., 2020), it should be remembered that these all crucially rely on Swarm's well established high quality data, either indirectly for essential validation or directly as a means of calibration. Given the good health of the instruments onboard the Swarm satellites there is therefore a strong argument that the Swarm mission should continue for as long as possible, extending the satellite geomagnetic time series and providing a stable backbone for new and more experimental missions. There are many clear benefits to having a long mission, in terms of data quality and having a reliable baseline, in terms of the carbon budget for space missions, and in terms of the increasing congestion of low-Earth-orbit space. Although Swarm Alpha and Charlie will inevitably reach the end of their lifetimes first due to their lower altitudes, from the standpoint of core field studies every effort should be made to extend the lifetime of Swarm Bravo for as long as possible.

CRediT authorship contribution statement

C.C. Finlay: Writing – original draft, Visualization, Project administration, Methodology, Investigation, Funding acquisition, Formal analysis, Conceptualization. C. Kloss: Writing – review & editing, Visualization, Software, Methodology, Investigation, Data curation. N. Gillet: Writing – review & editing, Validation, Software, Methodology, Investigation, Funding acquisition, Conceptualization.

Declaration of competing interest

The authors declare the following financial interests/personal relationships which may be considered as potential competing interests: CCF reports financial support was provided by European Space Agency. NG reports financial support was provided by European Space Agency. If there are other authors, they declare that they have no known competing financial interests or personal relationships that could have appeared to influence the work reported in this paper.

Acknowledgements

CCF thanks Nils Olsen and Lars Tøffner Clausen for helpful discussions. Julien Aubert is thanked for providing geodynamo simulation data. The European Space Agency (ESA) is thanked for providing

prompt access to the *Swarm* L1b satellite data. This work was supported by ESA under the EO Science for Society programme, through contract 4000127193/19/NL/IA (Swarm +4D Deep Earth: Core). Two anonymous reviewers are thanked for their constructive comments that helped improve the manuscript.

Data availability

The Swarm satellite data used in this are available from https://swarm-diss.eo.esa.int/. The field model constructed and analysed in this study is archived at https://data.dtu.dk/.

References

Alken, P., Thébault, E., Beggan, C.D., Amit, H., Aubert, J., Baerenzung, J., Bondar, T.N., Brown, W.J., Califf, S., Chambodut, A., Chulliat, A., Cox, G.A., Finlay, C.C., Fournier, A., Gillet, N., Grayver, A., Hammer, M.D., Holschneider, M., Huder, L., Hulot, G., Jager, T., Kloss, C., Korte, M., Kuang, W., Kuvshinov, A., Langlais, B., Léger, J.-M., Lesur, V., Livermore, P.W., Lowes, F.J., Macmillan, S., Magnes, W., Mandea, M., Marsal, S., Matzka, J., Metman, M.C., Minami, T., Morschhauser, A., Mound, J.E., Nair, M., Nakano, S., Olsen, N., Pavón-Carrasco, F.J., Petrov, V.G., Ropp, G., Rother, M., Sabaka, T.J., Sanchez, S., Saturnino, D., Schnepf, N.R., Shen, X., Stolle, C., Tangborn, A., Tøffner-Clausen, L., Toh, H., Torta, J.M., Varner, J., Vervelidou, F., Vigneron, P., Wardinski, I., Wicht, J., Woods, A., Yang, Y., Zeren, Z., Zhou, B., 2021. International geomagnetic reference field: the thirteenth generation. Earth, Planets Space 73 (1), 49. http://dx.doi.org/10.1186/s40623-020-01288-x.

Amit, H., Terra-Nova, F., Lézin, M., Trindade, R.I., 2021. Non-monotonic growth and motion of the south atlantic anomaly. Earth, Planets Space 73, 1–10. http://dx.doi.org/10.1186/s40623-021-01356-w.

Aubert, J., 2015. Geomagnetic forecasts driven by thermal wind dynamics in the Earth's core. Geophys. J. Int. 203 (3), 1738–1751. http://dx.doi.org/10.1093/gji/ggv394. Aubert, J., 2019. Approaching Earth's core conditions in high-resolution geodynamo simulations. Geophys. J. Int. 219 (Supplement_1), S137–S151. http://dx.doi.org/10.1093/gji/ggz232.

Aubert, J., 2020. Recent geomagnetic variations and the force balance in Earth's core. Geophys. J. Int. 221, 378–393. http://dx.doi.org/10.1093/gji/ggaa007.

Aubert, J., 2023. State and evolution of the geodynamo from numerical models reaching the physical conditions of Earth's core. Geophys. J. Int. http://dx.doi.org/10.1093/gji/ggad229.

Aubert, J., Gastine, T., Fournier, A., 2017. Spherical convective dynamos in the rapidly rotating asymptotic regime. J. Fluid. Mech. 813, 558–593. http://dx.doi.org/10. 1017/ffm.2016.789.

Aubert, J., Gillet, N., 2021. The interplay of fast waves and slow convection in geodynamo simulations nearing Earth's core conditions. Geophys. J. Int. 225, 1854–1873. http://dx.doi.org/10.1093/gji/ggab054.

Aubert, J., Livermore, P.W., Finlay, C.C., Fournier, A., Gillet, N., 2022. A taxonomy of simulated geomagnetic jerks. Geophys. J. Int. 231, 650–671. http://dx.doi.org/10. 1093/gii/ggac212.

Backus, G., Parker, R.L., Constable, C.G., 1996. Foundations of Geomagnetism. Cambridge Univ. Press, New York.

- Baerenzung, J., Holschneider, M., Saynish-Wagner, J., Thomas, M., 2022. Kalmag: a high spatio-temporal model of the geomagnetic feld. Earth, Planets Space 74, 139. http://dx.doi.org/10.1186/s40623-022-01692-5.
- Bloxham, J., 1986. The expulsion of magnetic flux from the Earth's core. Geophys. J. R. Astron. Soc. 87 (2), 669–678. http://dx.doi.org/10.1111/j.1365-246X.1986.
- Brauer, P., Merayo, J., Risbo, T., Primdahl, F., 2001. Magnetic Calibration Of Vector Magnetometers: Linearity, Thermal Effects and Stability, ESA SP-490. In: Primdahl, F., Balogh, A. (Eds.), Ground and in-Flight Space Magnetometer Calibration Techniques.
- Brekke, A., Egeland, A., 1986. Christopher Hansteen (1784–1873): A pioneer in the study of terrestrial magnetism. Eos, Trans. Am. Geophys. Union 67 (15), 185–187. http://dx.doi.org/10.1029/E0067i015p00185.
- Campuzano, S., Pavón-Carrasco, F.J., De Santis, A., González-López, A., Qamili, E., 2021. South atlantic anomaly areal extent as a possible indicator of geomagnetic jerks in the satellite era. Front. Earth Sci. 8, 607049. http://dx.doi.org/10.3389/ feart.2020.607049.
- Chulliat, A., Maus, S., 2014. Geomagnetic secular acceleration, jerks, and a localized standing wave at the core surface from 2000 to 2010. J. Geophys. Res. 119 (3), 1531–1543. http://dx.doi.org/10.1002/2013JB010604.
- Constable, C.G., 1988. Parameter estimation in non-Gaussian noise. Geophys. J. Int. 94 (1), 131–142. http://dx.doi.org/10.1111/j.1365-246X.1988.tb03433.x.
- Deconinck, F., Hulot, G., Léger, J.M., Clausen, L.B.N., Pastena, M., Lejault, J.P., Wilkinson, J., Caballero, D.M., Tostado, M.V., Coïsson, P., Jager, T., Nieto, P., Jørgensen, J.L., 2025. NanoMagSat status: a 3x16U low-Earth orbit constellation to monitor the Earth magnetic field and the ionospheric environment. In: Petrozzillstad, M. (Ed.), In: Small Satellites Systems and Services Symposium (4S 2024), vol. 13546, International Society for Optics and Photonics, SPIE, p. 135462K. http://dx.doi.org/10.1117/12.3062471.
- Finlay, C.C., Gillet, N., Aubert, J., Livermore, P.W., Jault, D., 2023. Gyres, jets and waves in the Earth's core. Nat. Rev. Earth Environ. 4, 377–392. http://dx.doi.org/ 10.1038/s43017-023-00425-w.
- Finlay, C.C., Kloss, C., Olsen, N., Hammer, M.D., Tøffner-Clausen, L., 2020. The CHAOS-7 geomagnetic field model and observed changes in the South Atlantic Anomaly. Earth, Planets Space 72 (156), http://dx.doi.org/10.1186/s40623-020-01252-9.
- Finlay, C.C., Olsen, N., Toffner-Clausen, L., 2015. DTU candidate field models for IGRF-12 and the CHAOS-5 geomagnetic field model. Earth. Planets. Space. 67, 114. http://dx.doi.org/10.1186/s40623-015-0274-3.
- Friis-Christensen, E., Lühr, H., Hulot, G., 2006. Swarm: A constellation to study the Earth's magnetic field. Earth, Planets Space 58 (4), 351–358. http://dx.doi.org/10. 1186/BF03351933.
- Gerick, F., Livermore, P., 2024. Interannual magneto-coriolis modes and their sensitivity on the magnetic field within the Earth's core. Proc. Royal Soc. A 480 (2299), 20240184. http://dx.doi.org/10.1098/rspa.2024.0184.
- Gillet, N., Dall'Asta, F., Amblard, P.O., Claveau, R., Aubert, J., 2024. Waves in Earth's core and geomagnetic field forecast. Phys. Earth Planet. Inter. 357, 107284. http://dx.doi.org/10.1016/j.pepi.2024.107284.
- Gillet, N., Gerick, F., Jault, D., Schwaiger, T., Aubert, J., Istas, M., 2022. Satellite magnetic data reveal interannual waves in Earth's core. Proc. Natl. Acad. Sci. 119, e2115258119. http://dx.doi.org/10.1073/pnas.211525811.
- Gillet, N., Huder, L., Aubert, J., 2019. A reduced stochastic model of core surface dynamics based on geodynamo simulations. Geophys. J. Int. 219 (1), 522–539. http://dx.doi.org/10.1093/gii/ggz313.
- Ginzburg, V.L., Kurnosova, L.V., Logachev, V.I., Razorenov, A.A., 1962. Investigation of charged particle intensity during the flights of the second and third space ship. Planet. Space Sci., 9, 845–854. http://dx.doi.org/10.1016/0032-0633(62)90113-7.
- Grayver, A.V., Munch, F.D., Kuvshinov, A.V., Khan, A., Sabaka, T.J., Tøffner-Clausen, L., 2017. Joint inversion of satellite-detected tidal and magnetospheric signals constrains electrical conductivity and water content of the upper mantle and transition zone. Geophys. Res. Lett. 44 (12), 6074–6081. http://dx.doi.org/10.1002/2017GL073446.
- Gubbins, D., Roberts, N., 1983. Use of the frozen flux approximation in the interpretation of archaeomagnetic and palaeomagnetic data. Geophys. J. R. Astron. Soc. 73, 675–687. http://dx.doi.org/10.1111/j.1365-246X.1983.tb03339.x.
- Gull, S., Skilling, J., 1990. The MEMSYS5 user's manual. Maximum Entropy Data Consultants Ltd, Royston.
- Hansteen, C., 1819. Untersuchungen über den Magnetismus der Erde. Christiania, Gedruckt bey J. Lehmann und C. Gröndahl.
- Hobson, M.P., Lasenby, A.N., 1998. The entropic prior for distributions with positive and negative values. Mon. Not. R. Astron. Soc. 298 (3), 905–908. http://dx.doi.org/10.1046/j.1365-8711.1998.01707.x.
- Hulot, G., Léger, J.M., Vigneron, P., Jager, T., Bertrand, F., Coïsson, P., Deram, P., Boness, A., Tomasini, L., Faure, B., 2018. Nanosatellite high-precision magnetic missions enabled by advances in a stand-alone scalar/vector absolute magnetometer. In: IGARSS 2018 2018 IEEE International Geoscience and Remote Sensing Symposium. pp. 6320–6323. http://dx.doi.org/10.1109/IGARSS.2018.8517754.
- Istas, M., Gillet, N., Finlay, C., Hammer, M., Huder, L., 2023. Transient core surface dynamics from ground and satellite geomagnetic data. Geophys. J. Int. 233, 1890–1915. http://dx.doi.org/10.1093/gji/ggad039.

- Jackson, A., 2003. Intense equatorial flux spots on the surface of Earth's core. Nature 424, 760–763. http://dx.doi.org/10.1038/nature01879.
- Jackson, A., Constable, C., Gillet, N., 2007. Maximum entropy regularization of the geomagnetic core field inverse problem. Geophys. J. Int. 171, 995–1004. http: //dx.doi.org/10.1111/j.1365-246X.2007.03530.x.
- Jaynes, E., 2003. Probability Theory: The Logic of Science. Cambridge University Press.
- Jiang, Y., Finlay, C.C., Olsen, N., Tøffner-Clausen, L., Yan, Q., Zhang, K., 2024. Macau Scientific Satellite-1 initial magnetic field model. Geophys. Res. Lett. 51 (22), http://dx.doi.org/10.1029/2024GL112305, e2024GL112305.
- Jørgensen, P.S., Merayo, J.M., Risbo, T., 2001. A method for the determination of three Euler angles for the SAC-C satellite magnetic mapper probe instrument package. Sensors Actuators A: Phys. 95 (1), 1–7. http://dx.doi.org/10.1016/s0924-4247(01)00752-x.
- Kakad, A., Kakad, B., 2022. An audit of geomagnetic field in polar and south atlantic anomaly regions over two centuries. Adv. Space Res. 69 (5), 2142–2157. http: //dx.doi.org/10.1016/j.asr.2021.12.011.
- Leger, J.M., Bertrand, F., Jager, T., Le Prado, M., Fratter, I., Lalaurie, J.C., 2009. Swarm absolute scalar and vector magnetometer based on helium 4 optical pumping. Procedia Chem. 1 (1), 634–637. http://dx.doi.org/10.1016/j.proche.2009.07.158, Proceedings of the Eurosensors XXIII conference.
- Li, J., Lin, Y., Zhang, K., 2024. Dynamic mode decomposition of the core surface flow inverted from geomagnetic field models. Geophys. Res. Lett. 51 (1), http://dx.doi. org/10.1029/2023GL106362, e2023GL106362, e2023GL106362 2023GL106362.
- Livermore, P.W., Finlay, C.C., Bayliff, M., 2020. Recent north magnetic pole acceleration towards Siberia caused by flux lobe elongation. Nat. Geosci. 13, 387–391. http://dx.doi.org/10.1038/s41561-020-0570-9.
- Maisinger, K., Hobson, M., Lasenby, A., 2004. Maximum-entropy image reconstruction using wavelets. Mon. Not. R. Astron. Soc. 347, 339–354. http://dx.doi.org/10. 1111/j.1365-2966.2004.07216.x.
- Merayo, J.M.G., Jørgensen, J.L., Friis-Christensen, E., Brauer, P., Primdahl, F., Jørgensen, P.S., Allin, T.H., Denver, T., 2008. The swarm magnetometry package. In: Sandau, R., Röser, H.-., Valenzuela, A. (Eds.), Small Satellites for Earth Observation. Springer Netherlands, Dordrecht, pp. 143–151. http://dx.doi.org/10.1007/978-1-4020-6943-7 13.
- Olsen, N., Albini, G., Bouffard, J., Parrinello, T., Tøffner-Clausen, L., 2020. Magnetic observations from CryoSat-2: calibration and processing of satellite platform magnetometer data. Earth, Planets Space 72 (1), http://dx.doi.org/10.1186/s40623-020-01171-9.
- Olsen, N., Floberghagen, R., 2018. Exploring Geospace from Space: the Swarm Satellite Constellation Mission. Space Res. Today 203, 61–71. http://dx.doi.org/10.1016/j. srt.2018.11.017.
- Olsen, N., Friis-Christensen, E., Floberghagen, R., Alken, P., Beggan, C.D., Chulliat, A., Doornbos, E., da Encarnac, J.T., Hamilton, B., Hulot, G., van den IJssel, J., Kuvshinov, A., Lesur, V., Luehr, H., Macmillan, S., Maus, S., Noja, M., Olsen, P.E.H., Park, J., Plank, G., Puethe, C., Rauberg, J., Ritter, P., Rother, M., Sabaka, T.J., Schachtschneider, R., Sirol, O., Stolle, C., Thebault, E., Thomson, A.W.P., Toeffner-Clausen, L., Velimsky, J., Vigneron, P., Visser, P.N., 2013. The swarm satellite constellation application and research facility (SCARF) and swarm data products. Earth, Planets Space 65, 1189–1200. http://dx.doi.org/10.5047/eps.2013.07.001.
- Olsen, N., Lühr, H., Finlay, C.C., Sabaka, T.J., Michaelis, I., Rauberg, J., Tøffner-Clausen, L., 2014. The CHAOS-4 geomagnetic field model. Geophys. J. Int. 197 (2), 815–827. http://dx.doi.org/10.1093/gji/ggu033.
- Olsen, N., Lühr, H., Sabaka, T.J., Mandea, M., Rother, M., Tøffner-Clausen, L., Choi, S., 2006. CHAOS—a model of the Earth's magnetic field derived from CHAMP, Ørsted, and SAC-C magnetic satellite data. Geophys. J. Int. 166 (1), 67–75. http://dx.doi. org/10.1093/gii/ggu033.
- Olsen, N., Ravat, D., Finlay, C.C., Kother, L.K., 2017. LCS-1: a high-resolution global model of the lithospheric magnetic field derived from CHAMP and Swarm satellite observations. Geophys. J. Int. 211 (3), 1461–1477. http://dx.doi.org/10.1093/gji/ggx381.
- Otzen, M., Finlay, C.C., Kloss, C., 2024. Co-estimation of core and lithospheric magnetic fields by a maximum entropy method. Geophys. J. Int. 236 (3), 1646–1667. http://dx.doi.org/10.1093/gji/ggae008.
- Pichon, G., Aubert, J., Fournier, A., 2016. Coupled dynamics of Earth's geomagnetic westward drift and inner core super-rotation. Earth Planet. Sci. Lett. 437, 114–126. http://dx.doi.org/10.1016/j.epsl.2016.01.004.
- Primdahl, F., Jensen, P.A., 1982. Compact spherical coil for fluxgate magnetometer vector feedback. J. Phys. E: Sci. Instrum. 15 (2), 221. http://dx.doi.org/10.1088/0022-3735/15/2/015.
- Reich, K., Roussanova, E., 2015. Carl Friedrich Gauß und Christopher Hansteen ,Der Briefwechsel beider Gelehrten im historischen Kontext. De Gruyter Akademie Forschung, Berlin, München, Boston, http://dx.doi.org/10.1515/9783110347975.
- Rogers, H.F., Gillet, N., Aubert, J., Personnettaz, P., Mandea, M., 2025. Effects of geodynamo priors and geomagnetic data on inverted core surface flows. Phys. Earth Planet. Inter. 107323. http://dx.doi.org/10.1016/j.pepi.2025.107323.
- Ropp, G., Lesur, V., 2023. Mid-latitude and equatorial core surface flow variations derived from observatory and satellite magnetic data. Geophys. J. Int. http://dx. doi.org/10.1093/gji/ggad113, ggad113.

- Rother, M., Korte, M., Morschhauser, A., Vervelidou, F., Matzka, J., Stolle, C., 2021. The Mag. num core field model as a parent for IGRF-13, and the recent evolution of the South Atlantic Anomaly. Earth, Planets Space 73, 1–17. http://dx.doi.org/10.1186/s40623-020-01277-0.
- Sabaka, T.J., Hulot, G., Olsen, N., 2015. Mathematical properties relevant to geomagnetic field modeling. In: Handbook of Geomathematics. Springer, http://dx.doi.org/10.1007/978-3-642-54551-1_17.
- Sabaka, T.J., Olsen, N., Purucker, M.E., 2004. Extending comprehensive models of the Earth's magnetic field with Ørsted and CHAMP data. Geophys. J. Int. 159 (2), 521–547. http://dx.doi.org/10.1111/j.1365-246X.2004.02421.x.
- Sabaka, T.J., Tøffner-Clausen, L., Olsen, N., Finlay, C.C., 2020. CM6: A comprehensive geomagnetic field model derived from both CHAMP and swarm satellite observations. Earth, Planets Space 72, 80. http://dx.doi.org/10.1186/s40623-020-01210-5
- Sadhasivan, M., Constable, C., 2022. A new power spectrum and stochastic representation for the geomagnetic axial dipole. Geophys. J. Int. 231 (1), 15–26. http://dx.doi.org/10.1093/gji/ggac172.
- Schwaiger, T., Gillet, N., Jault, D., Istas, M., Mandea, M., 2024. Wave-like motions and torques in Earth's core as inferred from geomagnetic data: A synthetic study. Phys. Earth Planet. Inter. 346, 107104. http://dx.doi.org/10.1016/j.pepi.2023.107104.

- Shannon, C.E., 1948. A mathematical theory of communication. Bell Syst. Tech. J. 27 (3), 379–423. http://dx.doi.org/10.1002/j.1538-7305.1948.tb01338.x.
- Swarm DISC, 2025. https://earth.esa.int/eogateway/activities/swarm-disc. (Accessed 24 March 2025).
- Troyano, M., Fournier, A., Gallet, Y., Finlay, C.C., 2020. Imprint of magnetic flux expulsion at the core-mantle boundary on geomagnetic field intensity variations. Geophys. J. Int. 221 (3), 1984–2009. http://dx.doi.org/10.1093/gji/ggaa126.
- Vernov, S.N., Chudakov, A.E., 1960. Terrestrial corpuscular radiation and cosmic rays. Space Res. 1, 751–796.
- Whaler, K.A., Hammer, M.D., Finlay, C.C., Olsen, N., 2022. Core surface flow changes associated with the 2017 Pacific geomagnetic jerk. Geophys. Res. Lett. 49, http: //dx.doi.org/10.1029/2022GL098616, e2022GL098616.
- Yoshida, S., Ludwig, G.H., Van Allen, J.A., 1960. Distribution of trapped radiation in the geomagnetic field. J. Geophys. Res. (1896-1977) 65 (3), 807–813. http://dx.doi.org/10.1029/JZ065i003p00807.
- Zhang, K., 2023. A novel geomagnetic satellite constellation: Science and applications. Earth Planet. Phys. 7, 4–21. http://dx.doi.org/10.26464/epp2023019.